





Cite this: DOI: 10.1039/d4bm00827h

Preparation of viromimetic rod-like nanoparticle vaccines (RLNVax) and study of their humoral immune activation efficacy†

Zichao Huang,^{a,b} Zhenyi Zhu,^{a,b} Liping Liu,^{a,b} Wantong Song  ^{*a,b,c} and Xuesi Chen  ^{*a,b,c}

Virus-like nanoparticle vaccines can efficiently activate the humoral immune response by cross-linking B cell receptors with their surface multivalent antigen arrays. This structurally dependent mechanism makes it crucial to regulate and optimize structural parameters to enhance the efficacy of nanoparticle vaccines. In this study, we prepared nanoparticle vaccines with different aspect ratios by chemically modifying antigen proteins onto the surfaces of poly(amino acid) nanoparticles of various shapes (spherical, ellipsoidal, and rod-like). This allowed us to investigate the impact of structural anisotropy on the humoral immune activation efficacy of nanoparticle vaccines. Furthermore, the end-group molecules of poly(amino acid) materials possess aggregation-induced emission (AIE) properties, which facilitate monitoring the dynamics of nano-assemblies within the body. Results showed that rod-like nanoparticle vaccines (RLNVax) with a higher aspect ratio (AR = 5) exhibited greater lymph node draining efficiency and could elicit more effective B cell activation compared to conventional isotropic spherical nanoparticle vaccines. In a murine subcutaneous immunization model using ovalbumin (OVA) as a model antigen, RLNVax elicited antigen-specific antibody titers that were about 64 times and 4.6 times higher than those induced by free antigen proteins and spherical nanoparticle vaccines, respectively. Additionally, when combined with an aluminum adjuvant, antibody titers elicited by RLNVax were further enhanced by 4-fold. These findings indicate that the anisotropic rod-like structure is advantageous for improving the humoral immune activation efficacy of nanoparticle vaccines, providing significant insights for the design and optimization of next-generation nanoparticle vaccines.

Received 21st June 2024,
Accepted 19th August 2024
DOI: 10.1039/d4bm00827h

rsc.li/biomaterials-science

Introduction

Vaccines function by activating the body's immune recognition of antigenic information from pathogens such as viruses,¹ establishing a defense barrier against them.² A key challenge in vaccine design lies in effectively presenting critical antigenic information from pathogens and efficiently activating the body's recognition and response capabilities.^{3,4} Virus-like particle (VLP) vaccines are considered highly promising due to their ability to densely exhibit viral antigen proteins on nanoparticle surfaces,^{5–7} thereby reproducing pathogen-associated structural patterns (PASP) and efficiently activating humoral immune responses through B-cell receptor cross-linking.⁸

Numerous studies have reported that parameters such as surface antigen protein valences and types significantly influence the stimulatory effects of VLP vaccines.^{9–11} They have also demonstrated that regulating and optimizing these structural parameters are crucial for enhancing VLP vaccine efficacy. In addition to direct stimulatory effects, the delivery efficiency and kinetic processes of these particulate vaccines *in vivo* are equally important. Previous studies have shown that while increasing surface valences enhanced the stimulatory effects of VLP vaccines, excessively high valence may compromise particle stability *in vivo*, thereby reducing lymphatic drainage efficiency¹² and failing to achieve optimal immune stimulation.^{13,14} Adjusting particle shape may provide a reliable approach for optimizing the *in vivo* circulation behavior of VLP vaccines. Currently, most VLP vaccine designs are based on isotropic spherical structures, largely derived from concepts of spherical virus biomimicry.¹⁵ However, rod-like viruses are also typical viral types, and the anisotropic rod-like structures affect particle behavior in fluids and interactions with cells differently.^{3,16–18} Studies have shown that compared to spherical particles, rod-like particles could align themselves

^aKey Laboratory of Polymer Ecomaterials, Changchun Institute of Applied Chemistry, Chinese Academy of Sciences, Changchun, 130022, China

^bSchool of Applied Chemistry and Engineering, University of Science and Technology of China, Hefei, 230026, China

^cJilin Biomedical Polymers Engineering Laboratory, Changchun, 130022, China

† Electronic supplementary information (ESI) available. See DOI: <https://doi.org/10.1039/d4bm00827h>

along the direction of flow and rotate under fluid shear forces, resulting in faster transport and penetration capabilities *in vivo*.^{19–22} Therefore, constructing rod-like nanoparticle vaccines represents a promising strategy to further enhance the immune efficacy of VLP vaccines.^{23,24}

In this study, we used biodegradable polyglutamic acid materials as a framework to prepare poly(γ -benzyl-L-glutamate)-*b*-poly(ethylene glycol)-*N*-maleimide copolymers terminated with tetraphenylethylene (TPE) groups (TPE-PBLG-*b*-PEG-Mal). The TPE groups promote the assembly of PBLG molecular chains into nanorod structures *via* π - π stacking effects,²⁵ while the maleimide groups facilitate the modification of antigen proteins onto the hydrophilic PEG surface of nanorods through click chemistry with antigen proteins bearing free thiol groups,²⁶ thereby preparing rod-like nanoparticle vaccines (RLNVax) capable of displaying multivalent antigen proteins on their surface. Furthermore, TPE groups exhibit aggregation-induced emission (AIE) properties,²⁷ enabling the monitoring of nanorod assembly dynamics *in vivo* through AIE fluorescence signals. To further investigate the impact of anisotropy on VLP vaccine mechanisms and stimulatory effects, we employed a solvent co-assembly strategy²⁵ to prepare three types of nanoparticles with different aspect ratios (AR): spherical (AR = 1.0), ellipsoidal (AR = 2.2), and rod-like (AR = 5.0). Results indicated that compared to spherical and ellipsoidal vaccines, RLNVax achieved the highest lymphatic drainage efficiency and induced the highest levels of antigen-specific antibody titers *in vivo*. These findings suggest that increasing nanoparticle structural anisotropy enhances the *in vivo* dynamics of nanoparticle vaccines, thereby boosting their humoral immune stimulation efficacy. This framework provides new insights for the design and development of VLP vaccines.

Results and discussion

Synthesis of TPE-PBLG and TPE-PBLG-*b*-PEG-Mal materials

TPE-PBLG was synthesized by initiating the ring-opening polymerization of D-glutamic acid 5-benzyl ester *N*-carboxyanhydride (BLG-NCA) with 1-(4-aminophenyl)-1,2,2-triphenylethylene (TPE-NH₂) (Fig. 1A). The product was characterized by proton nuclear magnetic resonance (¹H NMR) spectroscopy (Fig. 1B). According to methods described in the literature,²⁵ the degree of polymerization of PBLG was calculated to be 24 based on the ratio of the peak areas at chemical shifts of 7.3 ppm and 5.0 ppm (Fig. S1†). Subsequently, the block copolymer TPE-PBLG-*b*-PEG-Mal was obtained by reacting the amino-terminated TPE-PBLG with maleimide and *N*-hydroxysuccinimide ester functionalized polyethylene glycol (Mal-PEG_{20k}-NHS) (Fig. 1C). It is crucial to perform this reaction at low temperatures to prevent the maleimide group from reacting with the amino groups and becoming inactive. The product was characterized by ¹H NMR spectroscopy (Fig. 1D), where the appearance of a peak at 3.5 ppm confirmed the successful conjugation of the PEG block.

Assembly and characterization of nanoparticles with different aspect ratios

TPE-PBLG materials can self-assemble into rod-like nanoparticles in dioxane solvent, leveraging the dipolar interactions of PBLG's α -helix and the π - π stacking effect of TPE molecules (Fig. 2A). These straight-sided rod-like structures can be observed *via* transmission electron microscopy (TEM) (Fig. 2C, TG-rod). After PEG block modification, the assembly morphology of TPE-PBLG-*b*-PEG-Mal undergoes noticeable changes (Fig. 2B). As shown in Fig. 2C, the rod-like nanoparticles assembled from TPE-PBLG-*b*-PEG-Mal (TG-rod)

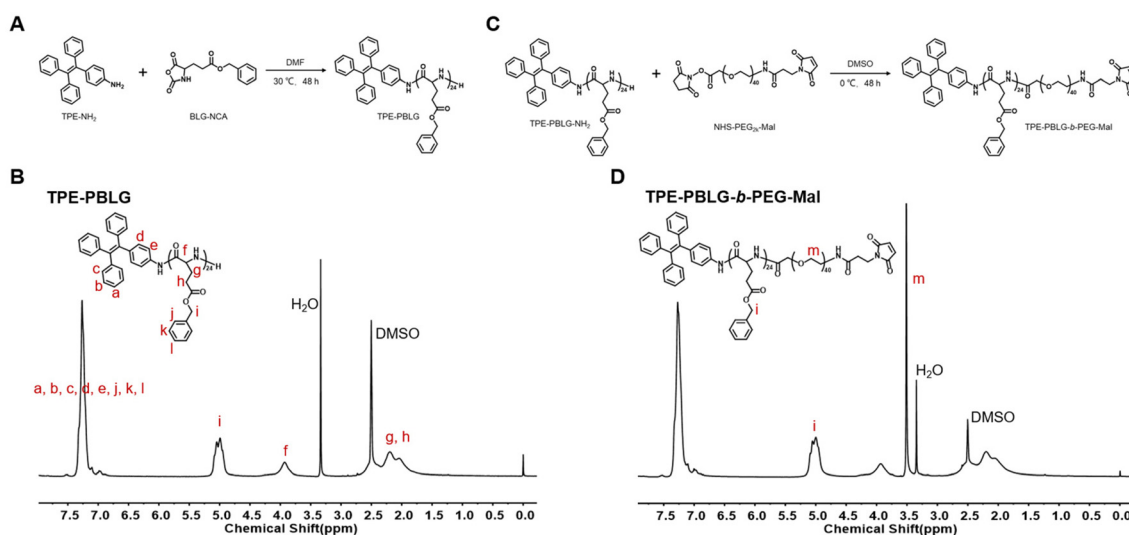


Fig. 1 Preparation and characterization of (A and B) TPE-PBLG and (C and D) TPE-PBLG-*b*-PEG-Mal. The degree of polymerization of TPE-PBLG was calculated to be approximately 24 based on the ratio of the peak areas of a, b, c, d, e, j, k, and l to peak i in the NMR spectrum. The appearance of peak m indicates the successful modification of PEG onto the PBLG terminal. The modification efficiency was determined to be approximately 20% based on the ratio of the peak areas of m to i.

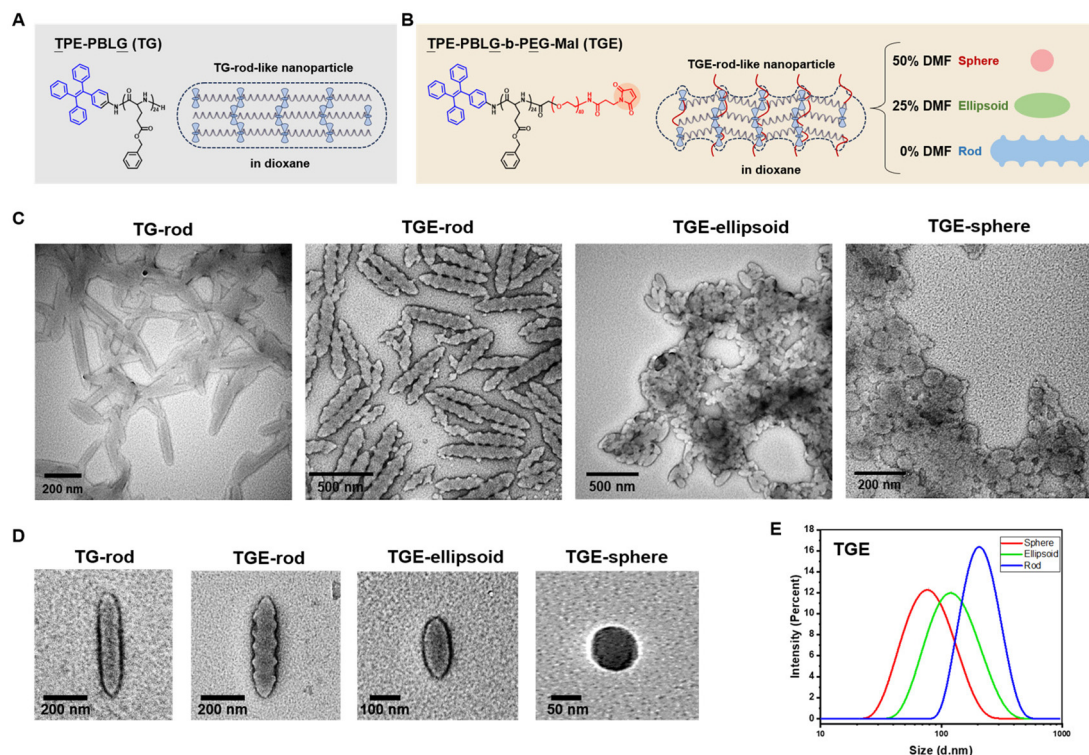


Fig. 2 Nano self-assembly using TPE-PBLG (TG) or TPE-PBLG-*b*-PEG-Mal (TGE) materials. (A) TPE-PBLG can adopt the head-to-tail (HTT) arrangement in helicogenic solvents such as dioxane, allowing for the assembly of rod-like nanoparticles. (B) Due to the hydrophilic PEG segments at the ends of the TPE-PBLG-*b*-PEG-Mal molecular chains, the assembled rod-like nanostructures may undergo some changes. Nanoparticles with different shapes (varying aspect ratios: spherical, ellipsoidal, and rod-like) can be prepared by adjusting the DMF proportion in the assembly solvent. (C) Transmission electron microscopy (TEM) characterization of the aggregation morphologies of nanoparticles with different shapes assembled from different materials. (D) High-resolution transmission electron microscopy characterization of the morphologies of individual nanoparticles with different shapes assembled from different materials. (E) Dynamic light scattering (DLS) characterization of the average hydrodynamic diameter of nanoparticles with different shapes assembled from TPE-PBLG-*b*-PEG-Mal.

exhibit wavy protrusions along their sides, likely due to the interference of the hydrophilic PEG blocks, which alter the original hydrophobic assembly morphology. TEM measurements indicated that the TPE-PBLG-*b*-PEG-Mal rod-like nanoparticles have a length of approximately 450 nm and a width of approximately 90 nm, resulting in an aspect ratio of 5.0 (Fig. 2D). Further control of the organic solvent components during the assembly process (the ratio of dioxane to DMF) allowed the formation of nanoparticles with different aspect ratios. When the DMF solvent ratio reached 25%, ellipsoid-like nanoparticles with a length of approximately 200 nm, a width of approximately 90 nm, and an aspect ratio of 2.2 were obtained (Fig. 2C and D). When the DMF solvent ratio reached 50%, spherical nanoparticles with both a length and width of approximately 80 nm and an aspect ratio of 1.0 were obtained. Dynamic light scattering (DLS) analysis of the hydrated particle sizes for the three different aspect ratios revealed that the measured data correspond to the average dimensions between the particle lengths and widths. The intensity-weighted particle sizes for rod-like, ellipsoid-like, and spherical particles are 220.3 ± 71.3 nm, 136.4 ± 62.0 nm, and 85.6 ± 38.0 nm, respectively (Fig. 2E).

Preparation and characterization of OVA-modified rod-like nanoparticle vaccines

Ovalbumin (OVA) was selected as the model antigen. OVA proteins were modified using 2-iminothiolane hydrochloride (Traut's reagent) to introduce free thiol groups. The modified antigen proteins were then co-incubated with the assembled rod-like nanoparticles. Through the click chemistry reaction between the thiol groups and the maleimide groups on the nanoparticle surface, the antigen proteins were successfully conjugated onto the nanoparticle surface (Fig. 3A). Previous work demonstrated that for spherical nanoparticle vaccines, an optimal surface valency existed that maximized *in vivo* lymphatic drainage efficiency and immune stimulation.¹³ To investigate whether rod-like nanoparticle vaccines offer advantages over spherical ones, we selected the optimal antigen-to-carrier material ratio for spherical vaccines ($1.7 \mu\text{g} : 1 \text{mg}$) for our rod-like nanoparticle preparation. The antigen modification efficiency on different nanoparticle carriers was assessed using ultrafiltration purification and BCA protein assay (Fig. 3B and Fig. S2†). Cryo-electron microscopy (cryo-EM) characterization of the antigen protein-rod-like nano-

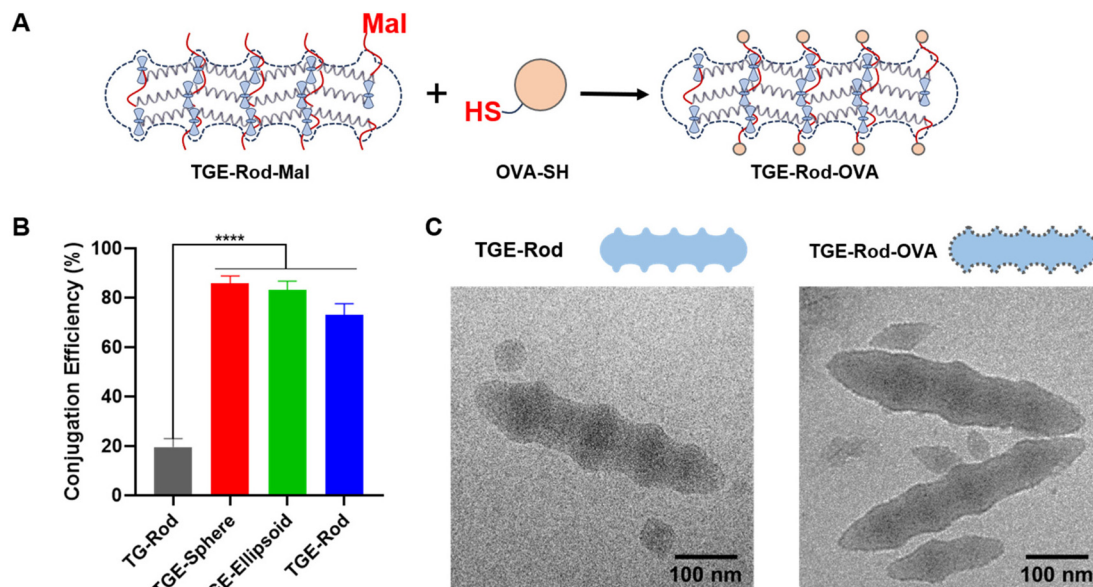


Fig. 3 Preparation of nanoparticle vaccines displaying surface antigen proteins. (A) The OVA antigen protein is modified using Traut's reagent to introduce free thiol groups, which can undergo a click reaction with the maleimide groups on the surface of TGE nanoparticles, thereby modifying the OVA protein onto the TGE nanoparticle surface. (B) Modification efficiency of the OVA antigen protein on the surface of nanoparticles with different shapes. Data were presented as mean \pm SD ($n = 3$) and were analyzed by Student's t -test. **** $p < 0.0001$. (C) Cryo-electron microscopy (cryo-EM) characterization of TGE rod-like nanoparticle vaccines with the surface-modified OVA antigen protein. The left image shows rod-like nanoparticles without protein modification, while the right image shows rod-like nanoparticles with protein modification.

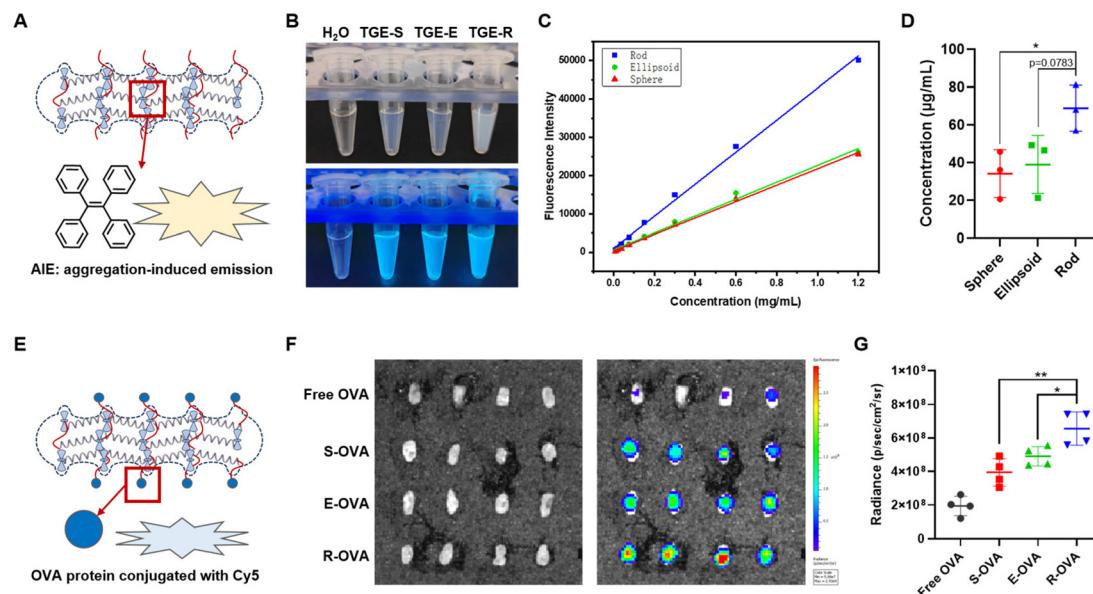


Fig. 4 *In vivo* lymph node drainage efficiency study of nanoparticle vaccines with different shapes. (A) Due to the presence of tetraphenylethylene groups, TGE materials assembled into nanoparticles exhibit aggregation-induced emission (AIE) properties, which can be used to monitor the fate of the assemblies *in vivo*. (B) Verification of the AIE phenomenon in solutions of TGE nanoparticles with different shapes under UV light illumination. S represents sphere, E represents ellipsoid, and R represents rod. (C) Standard curve of concentration vs. AIE fluorescence intensity for TGE nanoparticles with different shapes. Excitation wavelength: 350 nm, emission wavelength: 470 nm. (D) Concentrations of TGE nanoparticles with different shapes in 0.5 ml of lymph node homogenate supernatant calculated from AIE fluorescence intensity and the standard curve. Data were presented as mean \pm SD ($n = 3$) and were analyzed by Student's t -test. * $p < 0.05$. (E) By modifying TGE nanoparticles with the OVA protein conjugated with Cy5, the fate of TGE nanoparticle vaccines *in vivo* can be monitored via Cy5 fluorescence. (F) *Ex vivo* fluorescence imaging of draining lymph nodes after 24 hour treatment with OVA/Cy5 vaccines under different formulations. The left image is a bright-field image and the right image is a Cy5 fluorescence intensity image. Fluorescence intensity is expressed as radiance ($p \text{ sec}^{-1} \text{ cm}^{-2} \text{ sr}^{-1}$), with Min = 5.88e7 and Max = 2.93e9. S represents sphere, E represents ellipsoid, and R represents rod. (G) Quantitative analysis of Cy5 fluorescence intensity from (F). S represents sphere, E represents ellipsoid, and R represents rod. Data were presented as mean \pm SD ($n = 4$) and were analyzed by Student's t -test. * $p < 0.05$; ** $p < 0.01$.

particle conjugates (Fig. 3C) revealed rough particles on the surface of the rod-like nanoparticles after antigen protein reaction, indicating successful conjugation of the antigen proteins onto the surface of the rod-like nanoparticles. This confirms the successful preparation of rod-like nanoparticle vaccines. Nanoparticle vaccines of other shapes were also prepared using the same protocol, and their structural stability was assessed through particle size monitoring (Fig. S3†). The results indicate that nanoparticle vaccines of various shapes maintain size stability within 48 hours, while rod-like nanoparticles with protein modification exhibited a significant change in size at 72 hours.

Evaluation of lymph node drainage efficiency of nanoparticle vaccines with different aspect ratios

The efficiency with which vaccines drain to lymph nodes after entering the body is closely related to their effectiveness. Studies have indicated that particle size can affect the lymphatic drainage process of nanoparticles.¹⁷ To investigate the differences in lymph node drainage efficiency among nano-carriers of different shapes and sizes, equal masses of pure

carrier particles (spherical, ellipsoid, and rod-like) were subcutaneously injected into mice. The draining lymph nodes were harvested for analysis 24 hours post-injection. Due to the aggregation-induced emission (AIE) properties of TPE molecules (Fig. 4A and B), the concentration of the assemblies within the lymph nodes could be measured using AIE fluorescence signals. This AIE-based monitoring strategy ensures that the detected fluorescence signals originate from the assemblies rather than from degraded or dissociated free fluorescent molecules, which is a limitation of conventional methods that use conjugated fluorescent molecules for *in vivo* monitoring. After thoroughly grinding the harvested lymph node samples, the AIE fluorescence intensity of the grinding supernatant was measured using a plate reader (Fig. 4C). As shown in Fig. 4D and Fig. S4,† the AIE signal was strongest in the lymph node samples from the rod-like nanoparticle group, indicating that rod-like nanoparticles exhibited the highest lymph node drainage efficiency.

To further investigate the lymph node drainage efficiency of rod-like particles carrying antigen proteins, different shaped nanoparticle vaccines were prepared using OVA antigen pro-

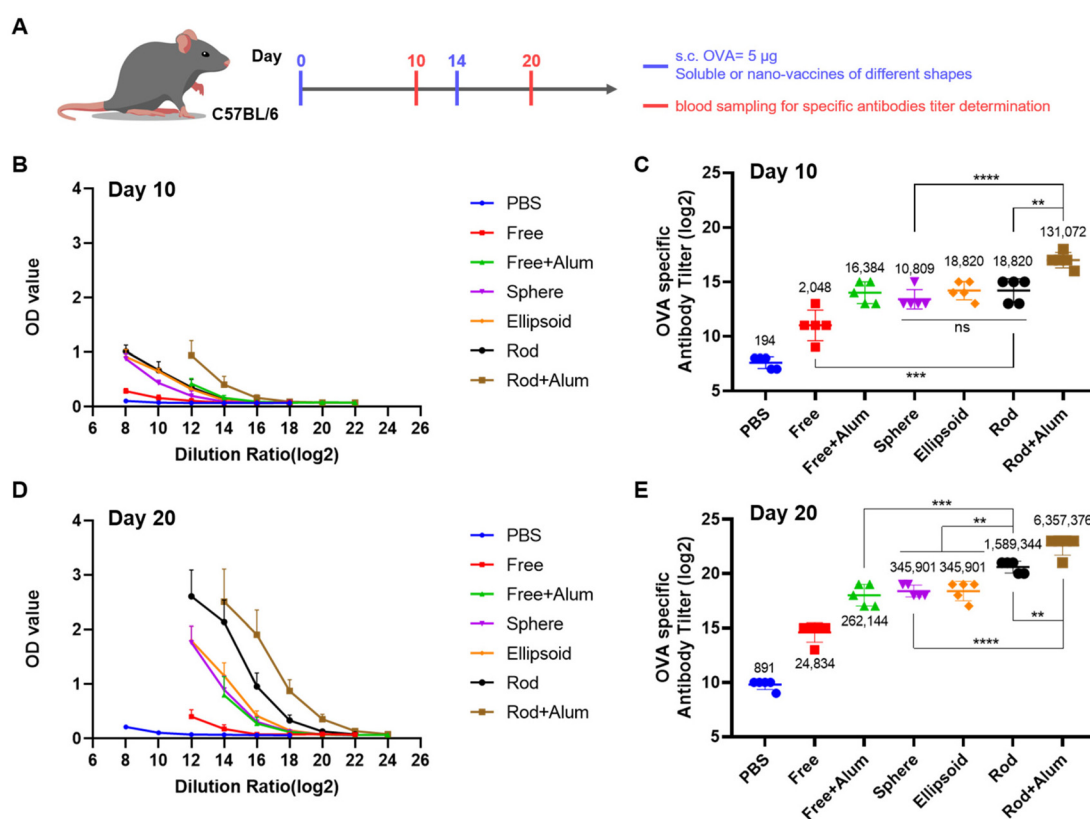


Fig. 5 Evaluation of humoral immune stimulation efficacy *in vivo* by nanoparticle vaccines of different shapes. (A) Subcutaneous immunization protocol of OVA vaccines in C57BL/6 mice. (B and C) OVA-specific IgG antibody endpoint titers of different treatment groups on day 10 (after a single dose on day 0). (B) Graphs showing the change in absorption intensity (OD value, optical density) vs. the dilution ratio (log 2) of sera in the specific antibody titer assay. (C) OVA-specific IgG antibody endpoint titers of different groups. Data were presented as mean \pm SD ($n = 5$) and were analyzed by Student's *t*-test. * $p < 0.05$; ** $p < 0.01$; *** $p < 0.001$; **** $p < 0.0001$. (D and E) OVA-specific IgG antibody endpoint titers of different treatment groups on day 20 (after prime-boost on day 14). (D) Graphs showing the change in absorption intensity (OD value, optical density) vs. the dilution ratio (log 2) of sera in the specific antibody titer assay. (E) OVA-specific IgG antibody endpoint titers of different groups. Data were presented as mean \pm SD ($n = 5$) and were analyzed by Student's *t*-test. * $p < 0.05$; ** $p < 0.01$; *** $p < 0.001$; **** $p < 0.0001$.

teins labeled with Cy5 fluorescent molecules (Fig. 4E). These vaccines were subcutaneously administered to mice, and the draining lymph nodes were harvested for *ex vivo* fluorescence imaging analysis 24 hours later (Fig. 4F). As shown in Fig. 4G, nanoparticle vaccines of all shapes had superior lymph node drainage efficiency compared to free antigen proteins, with the rod-like nanoparticle vaccines performing the best among the three shapes. In the lymph node drainage experiment conducted over 72 hours (Fig. S5[†]), the retention of nanoparticle vaccines in the lymph nodes decreased for all shapes compared to the 24 hour results. However, rod-like nanoparticle vaccines still exhibited a slight advantage in retention compared to other nanoparticle shapes. These results indicate that, compared to isotropic spherical nanoparticle vaccines, rod-like nanoparticle vaccines exhibit more advantageous lymphatic drainage efficiency *in vivo*. This advantage may be attributed to the anisotropic rod-like structure, which aligns in the flow and rotates and diffuses (enhancing transport speed)^{28,29} in fluid environments.

Evaluation of humoral immune activation efficiency of nanoparticle vaccines with different aspect ratios *in vivo*

OVA nanoparticle vaccines with different aspect ratios were prepared and administered to mice through two subcutaneous immunizations. Blood samples were collected on day 10 and day 20 post-immunization to measure the OVA-specific antibody titers (Fig. 5A). As shown in Fig. 5B, C and Fig. S7,† on day 10 after a single immunization, the antibody titers elicited by pure nanoparticle vaccines of different shapes were similar, reaching levels comparable to the free protein with alum adjuvant group (free OVA + Alum) and approximately 8 times higher than those elicited by the free antigen protein alone. The rod-like nanoparticle vaccine with alum adjuvant group (Fig. S6[†]) elicited even higher antibody titers, about 7 times higher than the pure rod-like nanoparticle vaccine without alum adjuvant. After the second booster immunization, as depicted in Fig. 5D, E and Fig. S8,† the antibody titers induced by spherical and ellipsoid nanoparticle vaccines remained similar, reaching levels comparable to the free protein with alum adjuvant group and approximately 13 times higher than those elicited by the free antigen protein alone. However, the rod-like nanoparticle vaccines demonstrated a significant advantage over vaccines of the other two shapes, eliciting antibody titers approximately 4.6 times higher than those of the spherical or ellipsoid nanoparticle vaccine groups. Additionally, the rod-like nanoparticle vaccines with the alum adjuvant group elicited antibody titers about 4 times higher than the pure rod-like nanoparticle vaccine group.

These results indicate that nanoparticle vaccines of different shapes can significantly enhance the stimulatory effect of the antigen protein. Among them, the rod-like nanoparticle vaccines exhibited superior humoral immune activation efficiency compared to vaccines of the other two shapes. Moreover, the combination with the alum adjuvant further enhanced the immune response elicited by the rod-like nanoparticle vaccine.

Conclusions

In this study, TPE-PBLG-*b*-PEG-Mal block copolymer materials with aggregation-induced emission (AIE) properties were used to construct nanoparticle vaccines with three different shapes (spherical, ellipsoid, and rod-like). Antigen proteins were conjugated to the surface of these nanoparticles through click chemistry, creating different-shaped nanoparticle vaccines. The lymphatic drainage efficiency of the nanoparticle vaccines was studied using the AIE properties of the assemblies, and the impact of structural anisotropy on the humoral immune stimulation efficacy of the nanoparticle vaccines was investigated in a mouse subcutaneous immunization model. The results showed that rod-like nanoparticle vaccines with a larger aspect ratio (AR = 5) exhibited the highest lymphatic drainage efficiency and induced the highest levels of antigen-specific antibody titers *in vivo*. Furthermore, combining the rod-like nanoparticle vaccines with an alum adjuvant further enhanced their efficacy. These findings indicate that the anisotropy of the structure affects the *in vivo* performance of nanoparticle vaccines. Adjusting the shape could be a new approach for enhancing the efficacy of existing nanoparticle vaccine platforms. However, this study only compared the effects of different shapes of nanoparticle vaccines at the same protein-to-material ratio and did not further investigate the differences in the efficacy of rod-like nanoparticle vaccines with varying surface valences.¹³ Moreover, considering the influence of size on the lymphatic circulation of nanoparticles, rod-like nanoparticles with larger lengths (micron-scale) may have difficulty draining back to the lymph nodes.^{30,31} Therefore, it is also necessary to study the impact of overall size, not just the aspect ratio, on the efficacy of rod-like nanoparticle vaccines.

Materials and methods

Materials

1-(4-Aminophenyl)-1,2,2-triphenylethylene, D-glutamic acid-5-benzyl ester-*N*-carboxyanhydride, and 2-iminothiophane hydrochloride were purchased from Shanghai Aladdin Biochemical Technology Co., Ltd. Anhydrous *n*-hexane, anhydrous tetrahydrofuran, and anhydrous dimethyl sulfoxide were obtained from Energy Chemical Reagent Co., Ltd. Mal-PEG2k-NHS was acquired from Shanghai Ponsure Biological Technology Co., Ltd. Cy5-NHS was obtained from Shanghai Yuanye Biotechnology Co., Ltd. Ovalbumin (OVA) was purchased from Sigma-Aldrich Trading Co. (Shanghai). Ultrafiltration tubes (10 kDa, 0.5 mL; 100 kDa, 0.5 mL; 100 kDa, 15 mL) were obtained from Merck Millipore. The BCA protein assay kit and anti-mouse IgG HRP antibody were purchased from Thermo Fisher Scientific. The TMB substrate was acquired from Beyotime Biotechnology. Female C57 BL/6 mice (6–8 weeks old) were purchased from Beijing Vital River Laboratory Animal Technology Co., Ltd. All animal experiments were conducted in accordance with the guidelines approved by the Animal Welfare and Ethics Committee of the

Changchun Institute of Applied Chemistry, Chinese Academy of Sciences (2022–0026).

Characterization

Nuclear magnetic resonance (NMR) spectra were characterized using a Bruker AV-300 NMR spectrometer. The average particle size of the nanoparticles was measured using a Zetasizer Nano ZS (Malvern Instruments Ltd). Transmission electron microscopy (TEM) images were obtained using a JEOL JEM-1011 (Tokyo, Japan). Cryo-transmission electron microscopy (cryo-TEM) images were acquired using a JEOL JEM-3200FSC (Tokyo, Japan). Absorbance measurements in 96-well plates were performed using a SPARK® multimode microplate reader. *Ex vivo* fluorescence images were captured using an IVIS Lumina LT III imaging system (PerkinElmer, USA).

Preparation and characterization of TPE-PBLG and TPE-PBLG-*b*-PEG-Mal materials

D-Glutamic acid-5-benzyl ester-*N*-carboxyanhydride (BLG-NCA) was recrystallized three times using a mixed solvent of anhydrous *n*-hexane and anhydrous tetrahydrofuran (1:3) to remove moisture from the NCA monomer. 1-(4-Aminophenyl)-1,2,2-triphenylethylene (TPE-NH₂) (50 mg) and BLG-NCA (760 mg) were dissolved in 7.5 mL of anhydrous DMF and stirred under low vacuum at 30 °C for 48 hours. Upon completion of the reaction, the product was precipitated three times using diethyl ether and then dried in a vacuum desiccator for 24 hours to obtain the TPE-PBLG solid. Samples were dissolved in deuterated dimethyl sulfoxide for proton nuclear magnetic resonance (NMR) spectroscopy analysis.

TPE-PBLG and NHS-PEG2k-Mal were dissolved in anhydrous DMSO at a molar ratio of 1:1.5 and stirred in an ice bath for 48 hours. After the reaction was completed, the mixture was dialyzed against deionized water for 72 hours using a dialysis bag with a molecular weight cutoff (MWCO) of 3500 Da, followed by lyophilization to obtain the TPE-PBLG-*b*-PEG-Mal solid. Samples were dissolved in deuterated dimethyl sulfoxide for proton NMR spectroscopy analysis.

Assembly and characterization of nanoparticles with different aspect ratios

To prepare rod-like nanoparticles, TPE-PBLG or TPE-PBLG-*b*-PEG-Mal materials were fully dissolved in dioxane at a concentration of 5 mg mL⁻¹ and aged for 48 hours. After aging, the organic phase solution was mixed with deionized water at a ratio of 1:3 under stirring, followed by dialysis against deionized water for 72 hours using a dialysis bag with a MWCO of 3500 Da. The resulting solution was then concentrated using a 100 kDa ultrafiltration tube.

For ellipsoid-like and spherical nanoparticles, the organic solvent used during the aging process was replaced with a mixed solvent containing 25% and 50% DMF, respectively, and the subsequent steps were the same as described above. The obtained nanoparticle solutions were drop-cast onto copper grids for transmission electron microscopy (TEM) imaging or directly subjected to dynamic light scattering (DLS) particle size analysis.

Preparation of nanoparticle vaccines surface-modified with the OVA antigen protein

The OVA antigen protein was first modified using a 5-fold molar excess of 2-iminothiophane hydrochloride in PB buffer (pH 8.5), followed by desalting through ultrafiltration. Subsequently, the modified OVA protein was mixed with a concentrated nanoparticle solution and incubated overnight at 4 °C with agitation. After incubation, purification was carried out using a 100 kDa ultrafiltration tube to remove unreacted OVA protein. The quantity of surface-modified OVA protein was quantified using a BCA protein assay kit to calculate the modification efficiency. The purified nanoparticle vaccine solution was then sampled for cryo-electron microscopy preparation to observe the distribution of the antigen protein on the nanoparticles.

Evaluation of *in vivo* lymph node drainage efficiency

For AIE fluorescence signal monitoring experiments, concentrated solutions of different shaped nanoparticles were subcutaneously injected into mice at a dose of 10 mg per 200 µL per injection. After 24 hours, mice were euthanized, and inguinal lymph nodes were harvested and soaked in 0.5 mL of deionized water. After thorough grinding of the lymph node tissue, the supernatant was filtered, and 0.2 mL was transferred to a 96-well plate for AIE fluorescence signal intensity measurement using an enzyme-linked immunosorbent assay reader (excitation wavelength: 350 nm, emission wavelength: 470 nm).

For Cy5 antigen protein fluorescence signal monitoring experiments, the OVA fluorescent protein was first labeled using Cy5-NHS, followed by ultrafiltration purification. The mass concentration of the OVA-Cy5 solution was determined using a BCA protein assay kit. Subsequently, the OVA-Cy5 protein was used in protein modification experiments to prepare nanoparticle vaccines surface-modified with OVA-Cy5. The quantified purified solutions of different shaped nanoparticles were subcutaneously injected into mice at a dose of 5 µg of OVA protein per 3 mg of material per 200 µL volume per injection. After 24 hours, mice were euthanized, and inguinal lymph nodes were imaged for Cy5 fluorescence signal intensity using an *ex vivo* fluorescence imaging system (excitation wavelength: 625 nm, emission wavelength: 670 nm).

Evaluation of *in vivo* OVA-specific antibody titers

Nanoparticle vaccines surface-modified with the OVA antigen protein of different shapes were prepared. On days 0 and 14, the quantified purified solutions of different shaped nanoparticles were subcutaneously injected into mice at a dose of 5 µg of OVA protein per 3 mg of material per 200 µL volume per injection. Blood samples were collected from the retro-orbital plexus on days 10 and 20, and serum was isolated to test OVA-specific antibody titers. Specifically, 100 µL of 10 µg mL⁻¹ OVA solution was pre-coated onto enzyme-linked immunosorbent assay plates and incubated overnight at 4 °C. After blocking with 2% BSA/PBS solution, serum samples were serially diluted in blocking buffer (starting with a 1:128

dilution, *i.e.*, adding 1.26 μL of serum to 160 μL of blocking buffer, followed by 4-fold serial dilutions). Diluted serum samples (100 μL) were added to washed ELISA plates and incubated for 2 hours. Anti-mouse IgG HRP antibody was then added according to the manufacturer's instructions and incubated for 1 hour. Finally, 100 μL of the TMB substrate was added and the resultant mixture was incubated at 37 °C for 10 minutes; then, the reaction was stopped with 100 μL of stop solution. The absorbance was measured at 450 nm to calculate the endpoint antibody titer data.

Data availability

The data supporting this article have been included as part of the ESI.†

Conflicts of interest

There are no conflicts to declare.

Acknowledgements

This work was supported by grants from the National Natural Science Foundation of China (Grant No. 22222509 and 22375198), the Jilin Province Science and Technology Development Plan (YDZJ202101ZYTS131 and 20220402037GH), the Jilin Provincial International Cooperation Key Laboratory of Biomedical Polymers (20210504001GH), the Changchun Science and Technology Development Plan (21ZY09), and the Youth Innovation Promotion Association of Chinese Academy of Sciences (2020232).

References

- Q.-F. Meng, W. Tai, M. Tian, X. Zhuang, Y. Pan, J. Lai, Y. Xu, Z. Xu, M. Li and G. Zhao, *Sci. Adv.*, 2023, **9**, eadg3277.
- M. F. Bachmann and G. T. Jennings, *Nat. Rev. Immunol.*, 2010, **10**, 787–796.
- M. O. Mohsen, G. Augusto and M. F. Bachmann, *Immunol. Rev.*, 2020, **296**, 155–168.
- J. Zhao, L. Liu, Y. Wang, Z. Huang, Y. Zhang, R. Qiao, T. P. Davis, Z. Tang, W. Song and X. Chen, *CCS Chem.*, 2024, **6**, 1278–1288.
- C. Zhao, Y. Pan, G. Yu, X. Z. Zhao, X. Chen and L. Rao, *Adv. Mater.*, 2023, **35**, 2207875.
- N. Butkovich, J. A. Tucker, A. Ramirez, E. Li, V. S. Meli, E. L. Nelson and S.-W. Wang, *Biomater. Sci.*, 2023, **11**, 596–610.
- Y.-R. Xue, Y. Wang, G. Chen, B. Sun, B. Li, L. Wu and Y. Wu, *Biomater. Sci.*, 2021, **9**, 3875–3883.
- M. F. Bachmann, M. O. Mohsen, L. Zha, M. Vogel and D. E. Speiser, *npj Vaccines*, 2021, **6**, 2.
- R. Veneziano, T. J. Moyer, M. B. Stone, E. C. Wamhoff, B. J. Read, S. Mukherjee, T. R. Shepherd, J. Das, W. R. Schief, D. J. Irvine and M. Bathe, *Nat. Nanotechnol.*, 2020, **15**, 716–723.
- J. Zhang, Y. Xu, M. Chen, Y. Huang, T. Song, C. Yang, Y. Yang and Y. Song, *J. Am. Chem. Soc.*, 2022, **144**, 21295–21303.
- A. A. Cohen, N. van Doremalen, A. J. Greaney, H. Andersen, A. Sharma, T. N. Starr, J. R. Keeffe, C. Fan, J. E. Schulz and P. N. Gnanapragasam, *Science*, 2022, **377**, eabq0839.
- L. Liu, J. Zhao, Z. Huang, Y. Xu, H. Chen, R. Qiao, W. Song, Z. Tang, T. P. Davis and X. Chen, *Fundam. Res.*, 2023, DOI: [10.1016/j.fmre.2023.03.018](https://doi.org/10.1016/j.fmre.2023.03.018).
- Z. Huang, X. Zhuang, L. Liu, J. Zhao, S. Ma, X. Si, Z. Zhu, F. Wu, N. Jin, M. Tian, W. Song and X. Chen, *Natl. Sci. Rev.*, 2023, **11**, nwad310.
- Y.-N. Zhang, S. Auclair and J. Zhu, *Natl. Sci. Rev.*, 2024, **11**, nwae032.
- M. O. Mohsen and M. F. Bachmann, *Cell. Mol. Immunol.*, 2022, **19**, 993–1011.
- C. Kinnear, T. L. Moore, L. Rodriguez-Lorenzo, B. Rothen-Rutishauser and A. Petri-Fink, *Chem. Rev.*, 2017, **117**, 11476–11521.
- S. Chattopadhyay, J.-Y. Chen, H.-W. Chen and C.-M. J. Hu, *Nanotheranostics*, 2017, **1**, 244.
- J. W. Stone, N. J. Thornburg, D. L. Blum, S. J. Kuhn, D. W. Wright and J. E. Crowe Jr, *Nanotechnology*, 2013, **24**, 295102.
- A. K. Pearce, T. R. Wilks, M. C. Arno and R. K. O'Reilly, *Nat. Rev. Chem.*, 2021, **5**, 21–45.
- Y. Geng, P. Dalhaimer, S. Cai, R. Tsai, M. Tewari, T. Minko and D. E. Discher, *Nat. Nanotechnol.*, 2007, **2**, 249–255.
- H. Almeida, G. Traverso, B. Sarmiento and J. das Neves, *Nat. Rev. Bioeng.*, 2024, 1–17.
- P. Cao, Z. P. Xu and L. Li, *Composites, Part B*, 2022, **236**, 109826.
- K. Niikura, T. Matsunaga, T. Suzuki, S. Kobayashi, H. Yamaguchi, Y. Orba, A. Kawaguchi, H. Hasegawa, K. Kajino and T. Ninomiya, *ACS Nano*, 2013, **7**, 3926–3938.
- X. Zottig, S. Al-Halifa, M. Côté-Cyr, C. Calzas, R. Le Goffic, C. Chevalier, D. Archambault and S. Bourgault, *Biomaterials*, 2021, **269**, 120672.
- J. Jiang, H. Sun, P. Wei, M. Sun, S. Lin, M. Lv, Z. Fan, Y. Zhu and J. Du, *Chem. Mater.*, 2022, **34**, 4937–4945.
- D. Wu, K. Yang, Z. Zhang, Y. Feng, L. Rao, X. Chen and G. Yu, *Chem. Soc. Rev.*, 2022, **51**, 1336–1376.
- J. Liu, H. Zhang, L. Hu, J. Wang, J. W. Lam, L. Blancafort and B. Tang, *J. Am. Chem. Soc.*, 2022, **144**, 7901–7910.
- M. J. Mitchell, M. M. Billingsley, R. M. Haley, M. E. Wechsler, N. A. Peppas and R. Langer, *Nat. Rev. Drug Discovery*, 2021, **20**, 101–124.
- W. Liu, L. Zhang, Z. Dong, K. Liu, H. He, Y. Lu, W. Wu and J. Qi, *Nano Res.*, 2022, **15**, 9243–9252.
- P. P. Wibroe, A. C. Anselmo, P. H. Nilsson, A. Sarode, V. Gupta, R. Urbanics, J. Szebeni, A. C. Hunter, S. Mitragotri and T. E. Mollnes, *Nat. Nanotechnol.*, 2017, **12**, 589–594.
- N. Benne, J. van Duijn, J. Kuiper, W. Jiskoot and B. Slütter, *J. Controlled Release*, 2016, **234**, 124–134.